Heliyon 10 (2024) e32094

Contents lists available at ScienceDirect

Heliyon

journal homepage: www.cell.com/heliyon

Research article

A coherent engineering assessment of ABS/biochar biocomposites in MEX 3D additive manufacturing

Nectarios Vidakis [a], Markos Petousis [a,*], Dimitrios Kalderis [b], Nikolaos Michailidis [c,d], Emmanuel Maravelakis [b], Vassilios Saltas [b], Nikolaos Bolanakis [b], Vassilis Papadakis [e,f], Apostolos Argyros [c,d], Nikolaos Mountakis [a], Mariza Spiridaki [a]

[a] Department of Mechanical Engineering, Hellenic Mediterranean University, Heraklion, 71410, Greece
[b] Department of Electronic Engineering, Hellenic Mediterranean University, Chania, 73133, Greece
[c] Physical Metallurgy Laboratory, Mechanical Engineering Department, School of Engineering, Aristotle University of Thessaloniki, 54124, Thessaloniki, Greece
[d] Centre for Research & Development of Advanced Materials (CERDAM), Center for Interdisciplinary Research and Innovation, Balkan Centre, Building B', 10th km Thessaloniki-Thermi Road, 57001, Thessaloniki, Greece
[e] Department of Industrial Design and Production Engineering, University of West Attica, 122 43, Athens, Greece
[f] Institute of Electronic Structure and Laser, Foundation for Research and Technology–Hellas, N. Plastira 100m, 70013, Heraklion, Greece

ARTICLE INFO

Keywords:
Acrylonitrile butadiene styrene
Biochar
Material extrusion
3D printing
Electrical conductivity
Mechanical performance

ABSTRACT

Acrylonitrile butadiene styrene (ABS) composites were prepared in filament form compatible with the material extrusion (MEX) 3D printing method, using biochar as a filler at various loadings of up to 10.0 wt %. Samples were fabricated to experimentally investigate their mechanical performance. The ABS/biochar composites were characterized using thermogravimetric analysis, differential scanning calorimetry, Raman spectroscopy, and rheological tests. The electrical properties of the composites were investigated using broadband dielectric spectroscopy. Scanning electron microscopy was utilized to analyze the morphological features of the fabricated specimens by examining their side and fracture surfaces. The results indicate that the composite with 4.0 wt % biochar content compared to pure ABS showed the highest mechanical response between the prepared composites (24.9 % and 21 % higher than the pure ABS tensile and flexural strength respectively). The composites retained their insulating behavior. These findings contribute to expanding the utilization of the material extrusion (MEX) 3D printing method while also unlocking prospects for potential applications in microelectronics, apart from mechanical reinforcement.

1. Introduction

Bioeconomy is of the foremost importance to have a positive impact on environmental protection. Sustainable biological sources are being explored and exploited using biotechnology to create new products and services. Biochar is a solid high-carbon biomass pyrolysis product. Some of the raw materials that can be used for biochar production are woody or organic waste, agricultural by-products, animal manure, and forestry residues [1]. Its composition can vary depending on the raw material from which it is

* Corresponding author.
E-mail address: markospetousis@hmu.gr (M. Petousis).

https://doi.org/10.1016/j.heliyon.2024.e32094
Received 31 January 2024; Received in revised form 27 May 2024; Accepted 28 May 2024
Available online 29 May 2024

derived and the pyrolysis conditions [2–4]. Its high carbon content, cation exchange capacity, stable structure, and large specific area are some of the advantageous characteristics that have attracted the attention of the research community [5]. During the thermomechanical decomposition of biomass, biochar production can reduce the amount of carbon emitted into the atmosphere and act as a carbon sink [6]. The use of biochar can be effective in both improving the economic viability and environmental sustainability of biomass-related thermochemical technologies [7]. The suitability of biochar for specific applications is determined based on its physicochemical properties. Some applications of biochar include water and air pollutant absorbents [4,8], catalysts for tar removal and biodiesel production [9,10], soil amendment [4,11], fuel cells [12,13], and supercapacitors [14,15].

Biochar with increased electrical conductivity, porosity, and stability is often utilized as an electrode material in microbial fuel cells [16], whereas a high number of oxygen-containing functional groups on its surface is advantageous for use in carbon fuel cells [17]. To develop efficient supercapacitors, biochar with a high porosity and low ash content is essential [18].

Strategies for achieving high-*k* dielectrics with low losses include the incorporation of various ceramic fillers and highly conductive particles such as metals of carbon-based materials in a polymer matrix. In the latter case, carbon nanotubes (CNT), multiwalled CNT, and graphene incorporated into polymers have been widely investigated to optimize the dielectric behavior to achieve high-*k* with low-loss composites [19–22]. Apart from carbon-based composites, other types of fillers have been investigated to induce dielectric properties in polymeric matrices such as acrylonitrile butadiene styrene (ABS) [23]. Biochar could be considered as a potential candidate to replace the high-cost production of dielectric composites. To the authors' best understanding, the electrical characterization of biochar/polymer composites is scarce. In 3D printing, biochar as an additive has been introduced in Polylactic Acid (PLA) [24] or High-Density Polyethylene (HDPE) [25] as the matrix materials in material extrusion (MEX) and standard grade resins in vat photopolymerization (VPP) [24] 3D printing. The aim was to evaluate the qualities it induces in the matrix materials, such as mechanical reinforcement, and electrical properties of the composites.

ABS is constantly utilized in various studies to examine its properties as a 3D printed polymer in the fused filament fabrication (FFF) MEX technique in pure [26,27] and composite forms [28,29]. It can be easily utilized by the user in 3D printing as its melting point is found at the low value of approximately 200 °C [30]. It also presents characteristics that can be beneficial for various printing applications, namely its chemical inertness, its ability to recycle, and its eco-friendliness [30], while also possessing excellent mechanical properties combined with lightweight quality [30]. It should be mentioned that several studies assess the ABS mechanical properties [31–33]. The cost of ABS when ordering over 1000 kg is approximately 0.35 €/kg. The respective commercial filament is priced at approximately 25 €. Therefore, the main cause of the high cost is the process of manufacturing the filament, rather than the expense of the matrix material itself. At the same time, it can be considered a sustainable polymer because it can withstand up to six successive thermomechanical processes without compromising its properties [34].

The rationale of this work was to combine ABS and biochar to develop composites with improved properties compared to ABS alone and simultaneously offer a sustainable valorization pathway for major agricultural residues. Biochar was prepared from olive tree pruning waste, an agricultural waste that is abundant in the Mediterranean region. The aim was to achieve optimal mechanical and

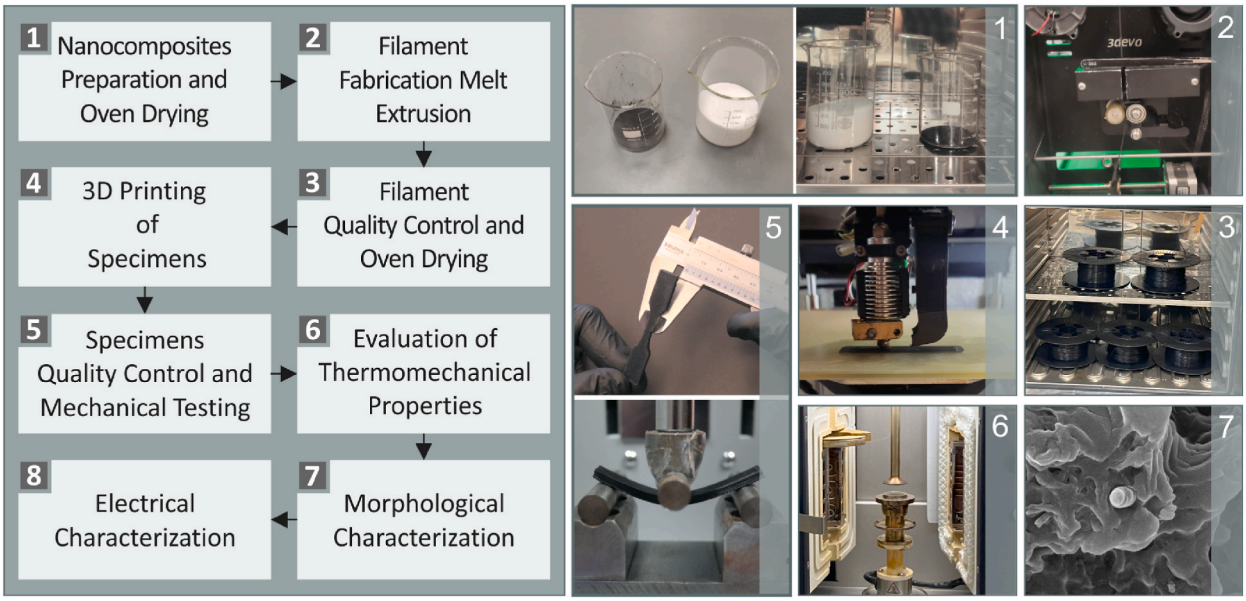

Fig. 1. Overview of the experimental steps. The pictures from the experimental process present: **(1)** composites composition and drying in the oven, **(2)** production of filament through melt extrusion, **(3)** quality control of the filament and drying in the oven, **(4)** fabrication of the 3D printed samples, **(5)** quality control and mechanical testing of the 3D printed samples, **(6)** thermomechanical properties evaluation, and **(7)** morphological characterization of the specimens. On the left side, a flowchart depecting the experimental steps of the research is presented, while on the right side, each step of the flowchart is visualized through respective pictures from the experimental process (the number in each box corresponds to an image with the same numer on the right side).

thermal characteristics of the composites to make them suitable for use in additive manufacturing (AM). Due to the presence of carbon in biochar, the produced composites are expected to have electrical properties, as well. Therefore, we investigated this effect. The creation of filaments from the different composites followed, which were subsequently utilized to fabricate samples for various tests aimed at assessing their mechanical, electrical, and rheological behavior, thermal quality, and morphological characteristics.

2. Materials and methods

The experimental steps followed are summarized in Fig. 1. First, the nanocomposites were prepared and left in an oven overnight to dry, followed by the fabrication of the filaments through melt extrusion. The fabricated filaments underwent quality control and were subsequently oven-dried. The specimens were then fabricated via 3D printing and subjected to quality control, mechanical testing, electrical characterization, thermomechanical evaluation, and morphological characterization.

2.1. Materials

The matrix material in the composites was ABS polymeric powder, purchased from INEOS Styrolution grade Terluran Hi-10 (INEOS Styrolution, Frankfurt, Germany). According to the supplier, the maximum tensile strength of ABS is 38 MPa, whereas its density is 1080 kg/m^3. For the production of biochar, olive tree pruning biomass was collected from Chania, Crete, and was then washed, and air-dried, with the aim of removing the existing impurities. Flame curtain pyrolysis was performed to create an olive tree-pruning biochar. A detailed account of biomass, pyrolysis equipment, and processes can be found elsewhere [35]. The pyrolysis temperature was maintained at 540 ± 50 °C throughout the process, as monitored by thermocouples attached to the exterior of the kiln. After quenching, the biochar was air-dried and ground in a sepor-type rod mill.

The particle size distribution of the biochar was determined in our earlier work [24]. The D(0,5) and D(0,9) values were 14.64 and 50.32 μm, respectively. The TermoFlash-2000 combustion analyzer (Thermo Fisher Scientific, UK) was used to carry out elemental analyses of C, H, N, and S content. The European Biochar Certificate (EBC) guidelines were followed to determine the ash content (EBC-2012, ver. 9.3 E), and the oxygen levels were calculated using the difference. The XRF (X-ray fluorescence spectrometry) was used to determine the chemical makeup of the samples (Rigaku ZSX Primull, Japan). The process for determining these specifications was presented in a previous study [24]. Scanning electron microscopy (SEM) was carried out on biochar samples using the JSM-IT700HR instrument from Jeol Ltd. in Tokyo, Japan.

2.2. ABS-biochar composites preparation

A blender with a high wattage was used to mix the ABS and biochar for 30 min at 4000 rpm. The mixtures were dried overnight in an oven before they were ready for fabrication into filaments. Six biochar loadings (0.0, 2.0, 4.0, 6.0, 8.0, and 10.0 wt %) of the ABS/biochar. The loading of biochar was increased gradually, as every composite underwent all the tests, and then the investigation proceeded to create the next composite with a higher biochar loading. This process continued until the mechanical performance of the samples reached its peak and began to decline, which allowed this study to investigate the performance of composites with a biochar

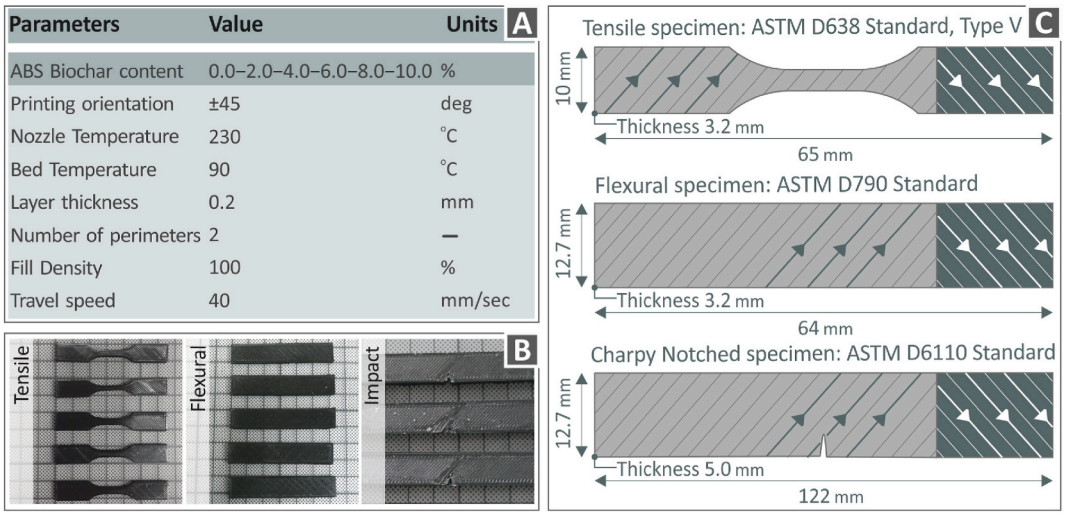

Fig. 2. (A) Presentation of the 3D printing settings utilized for the fabrication of the samples, (B) a selection of randomly chosen fabricated specimens and (C) an illustration depicting the geometry and dimensions of the specimens, following the corresponding standards. The arrows within the geometry denote the infill pattern utilized for constructing the 3D printing structure, with the orientation changing by 90° between successive layers.

loading of up to 10.0 wt %. It should be noted that in the specific study, the ABS raw material was in opaque ivory color, which is the natural color of ABS. With the addition of biochar, the composites became grey at the 2 and 4 wt % biochar loaded composites and then solid black at higher biochar loadings in the composites, which was somehow expected, due to the high content of carbon in biochar.

To achieve a uniform distribution of biochar particles in the matrix material, the filament was extruded twice. Initially, a Noztek Pro desktop single-screw extruder, manufactured by Noztek (Shoreham-by-Sea, United Kingdom), was utilized to convert the ABS-biochar mixture into filaments. Subsequently, a 3D Evo Shredder (3D Evo B.V., Utrecht, NL) was employed to transform the manufactured filament into pellets. Finally, the 3D Evo Precision 450 apparatus, also produced by 3D Evo B.V., was utilized due to its special screw that facilitated the mixing and melting of materials. The temperature on the heating zones of the extruder was from the first to the fourth: 220 °C, 230 °C, 230 °C and 240 °C, respectively. The rate at which the fan was operating was set at 55 %, while the speed at which the screw was turning was 3.5 revolutions per minute, achieving an average diameter of the filament of 1.75 mm. The filament produced with these specifications would be suitable for use in the specimens' fabrication with the MEX 3D printing technique. The 3D printing settings of the extrusion were chosen based on the results of preliminary tests and the respective ABS related to MEX 3D printing information provided in the literature [31].

2.3. Mechanical tests

An Imada MX2 testing apparatus (Imada Inc., Northbrook, IL, USA) was utilized to perform the tensile and flexural tests on the specimens, adhering to ASTM D638-14 (type V) and ASTM D790-10 standards, respectively. Charpy notched impact tests, as per ASTM D6110 standard, were conducted using a Terco MT220 (Terco AB, Kungens, Sweden), while a Vickers microhardness test, following ASTM E384-17 standard, was carried out using an Inova Test 300-Vickers device (Innovatest Europe BV, Maastricht, the Netherlands). In all experiments, five samples were tested per case, according to the instructions of the respective standard. All tests were carried out at room temperature (22 °C) conditions.

Fig. 2 illustrates the parameters for fabricating the 3D printed specimens (Fig. 2A), along with images of randomly selected fabricated specimens (Fig. 2B) and an illustration of their form and dimensions (Fig. 2C). The nozzle temperature was maintained at 230 °C, bed temperature at 90 °C, layer thickness at 0.2 mm, fill density at 100 %, and extrusion speed at 40 mm/s.

2.4. Raman spectroscopy

Raman spectroscopic analysis was performed using a LabRAM-HR Raman device (HORIBA Sci., Kyoto, Japan), with 1.7 μm and 2 μm lateral and axial microscope resolutions respectively, a 50 to 3900 cm^{-1} range of acquisition spectral scope, three demanding consecutive optical windows, 10 s exposure required time and five accumulations. Regarding the specifications of the system, 532 nm was the main laser line of the spectrometer, The excitation output power was set at 90 mW, and an Olympus objective lens (LMPlanFL N) with a numerical aperture of 0.5, magnification of 50 ×, and an operational working distance of 10.6 was utilized. The surface laser power of each sample was 2 mW.

2.5. Thermogravimetric (TGA) and differential scanning calorimetry (DSC) analyses

The analysis employed a PerkinElmer Diamond TGA/DTGA apparatus (PerkinElmer, Waltham, United States) for the investigation of the specimens' thermal properties, with a 10 °C/min temperature ramp (40–550 °C). Measurements were taken both in nitrogen (N) atmosphere and air for comparison purposes. The supply was adjusted at 200 ml/min in both cases. Measurements were conducted following the ASTM E1131 standard. The DSC measurements were conducted using a device called DSC 25 (TA Instruments, New Castle, United States) within the temperature span of 30–300 °C.

2.6. Scanning electron microscopy (SEM)

Morphological analysis of the test samples was performed by inspecting with SEM the fractured and side surfaces at various magnifications using a JSM-IT700HR field-emission SEM (Jeol Ltd., Tokyo, Japan).

2.7. Broadband dielectric spectroscopy

An Alpha-ANB high-resolution dielectric spectrometer (Novocontrol Technologies) was used to perform dielectric measurements of the ABS/biochar composites. A dielectric analyzer was used in conjunction with the ZGS Alpha Active sample holder and the BDS 1100 module, which ensured accurate, low-noise, and high-repeatability measurements over a wide range of frequencies. WinDeta software was used for system control and data acquisition. Circular disc-shaped compression-molded specimens were prepared with a diameter of 40 mm and a thickness of 4 mm. The specimen constituted the dielectric material of a sandwich-structured capacitor in a two-electrode configuration. The silver conductive paste was applied on both sides of each specimen to enhance electrical contact with the gold-plated electrodes of the sample holder. The measurements were performed in the frequency range, of $10^{-2} \times 4 \times 10^{6}$ Hz, at room temperature (25 °C). The results were expressed as complex functions of the dielectric permittivity $\varepsilon^*(\omega)$ (equation (1)), complex impedance $\sigma^*(\omega)$ (equation (2)), and dissipation factor $\tan(\delta)$ (equation (3)). These quantities are interrelated through the following relations:

$$\varepsilon^*(\omega) = \varepsilon' - i\varepsilon'' = \frac{C(\omega)}{\varepsilon_o \pi r^2/d} - i\frac{1}{\omega R(\omega)\varepsilon_o \pi r^2/d} \quad (1)$$

$$\sigma^*(\omega) = \sigma' - i\sigma'' = i\omega\varepsilon_o(\varepsilon^*(\omega) - 1) = \omega\varepsilon_o\varepsilon'' - i\omega\varepsilon_o(\varepsilon' - 1) \quad (2)$$

and

$$\tan(\delta) = \frac{\varepsilon''}{\varepsilon'} \quad (3)$$

where the output values of the analyzer are the resistance R(ω) and the capacitance C(ω), d is the specimen thickness r is its radius, $\omega = 2\pi f$ is the angular frequency and ε_o is the permittivity of the vacuum. The real part ε' of the complex permittivity is a direct measure of the energy storage in the material owing to the applied electric field, whereas the imaginary part ε'' is associated with the material's energy loss.

3. Results

3.1. Raman spectra of ABS/biochar composites

Fig. 3A shows the Raman spectra from the analysis of pure ABS and all ABS/biochar composites at 2.0, 4.0, 6.0, 8.0, and 10.0 wt % filler content. Fig. 3B shows the same spectra after subtraction of the spectrum of pure ABS. It is evident that all Raman peaks stem from pure ABS. The corresponding Raman signals are detailed in Table 1 and corroborated in the literature.

The progressive addition of biochar produced two peaks, one between 1245 and 1410 with a central wavelength of 1350 cm^{-1}. This wavelength is described in the literature as the graphite D band of disordered graphite, and the second is between 1520 and 1660 cm^{-1} with a central wavelength of 1590 cm^{-1}, which is also described in the literature as the G-band of ordered graphite. The intensity of these peaks increased with increasing biochar loading and was more prominent at biochar loadings of 6.0, 8.0, and 10.0 wt %.

3.2. TGA and DSC results

Fig. 4A presents the temperature dependence of the mass of pure ABS and all ABS/biochar composites. The graphs taken in N atmosphere (solid lines) and in air (dotted lines) are presented. As shown, in the measurements taken in air the acute degradation of the samples begins at slightly lower temperatures, following a similar pattern with the measurements taken in N atmosphere. The main difference is in the higher temperatures, in which the curves that were taken in air significantly differ and the residual mass decreases.

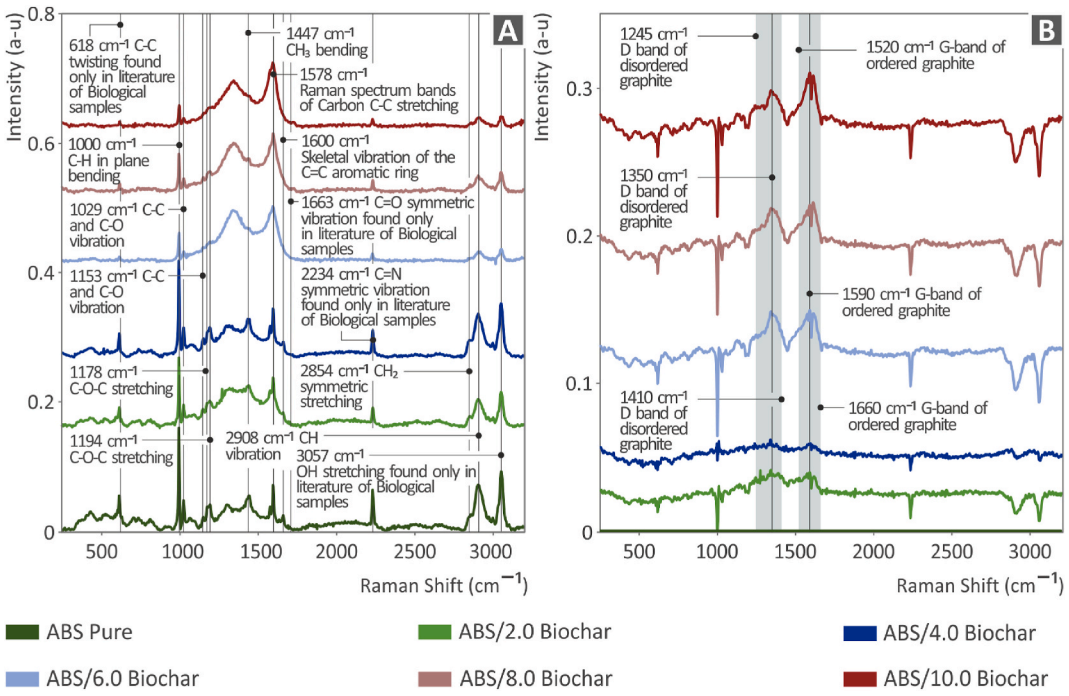

Fig. 3. Presentation of **(A)** Raman spectra (pure ABS and ABS/biochar composites), **(B)** the subtraction of pure ABS from all ABS/biochar composites.

Table 1
Major Raman peaks of pure ABS identified and their related assignments.

Wavenumber (cm^{-1})	Raman peak assignment
618	C-C twisting was found only in bio-based samples [36]
1000	C-H in-plane bending [37]
1029	C–C and C-O vibration [38]
1153	Antisymmetric Si-O- stretch [39]
1178	C-O-C stretching [37]
1194	C-O-C stretching [40]
1447	CH_3 bending [41–43]
1578	Raman spectrum bands of Carbon C-C stretching [44]
1600	Skeletal vibration of the C═C aromatic ring [45,46]
1663	C═O symmetric vibration found only in the literature of biological samples [36]
2234	C≡ N stretching vibrations found only in the literature of biological samples [36]
2854	CH_2 symmetric stretching [38]
2908	CH vibration [38]
3057	OH stretching found only in the literature on biological samples [36]

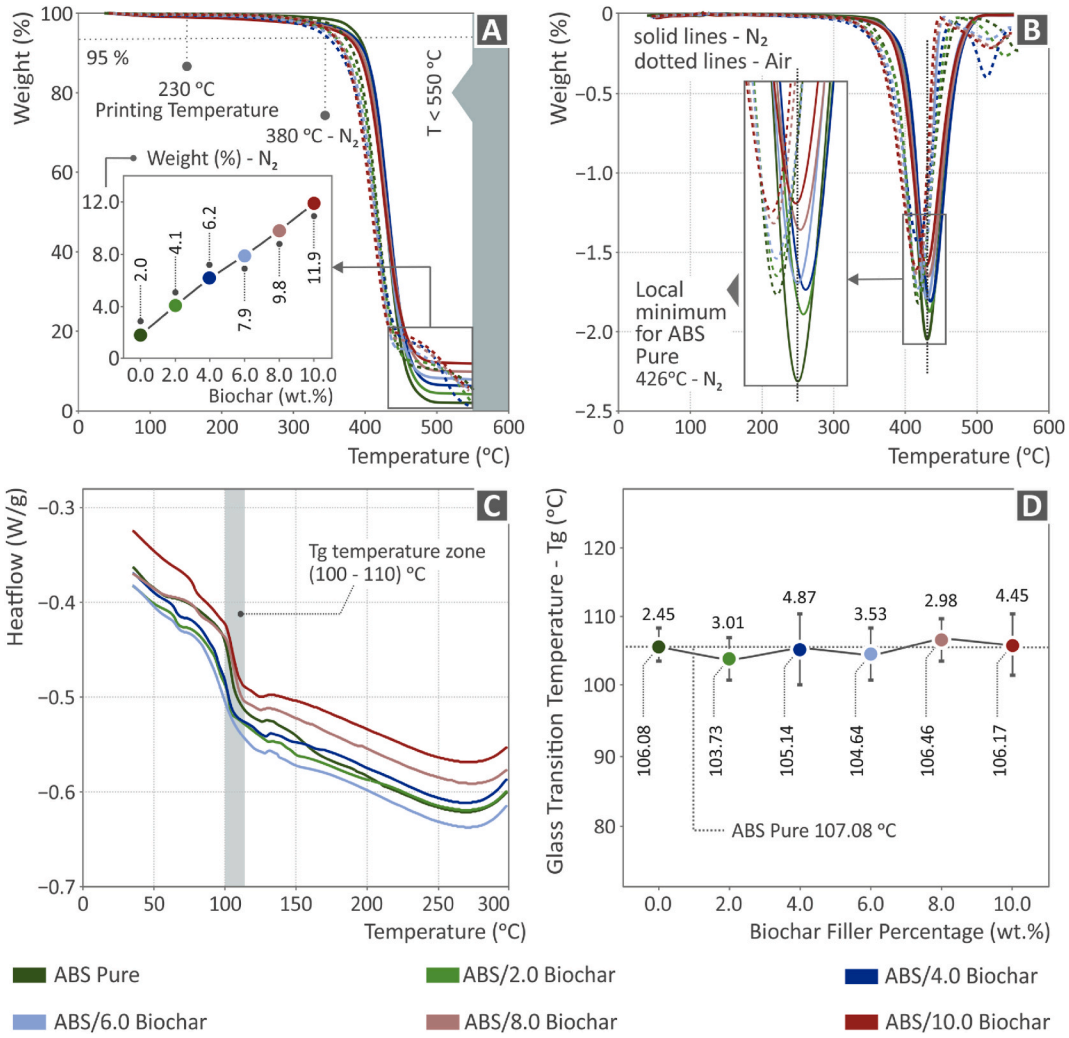

Fig. 4. Graph of **(A)** weight vs. temperature (TGA, and residual mass in the inset graph for the measurements taken in N atmosphere, solid lines present the measurements taken at N atmosphere and dotted lines the respective measurements in air), **(B)** DTG curves (solid lines present the measurements taken at N atmosphere and dotted lines the respective measurements in air), **(C)** heat flow compared to temperature derived on the DSC analysis for pure ABS and ABS/biochar composites, **(D)** Glass transition temperatures Tg (°C) measured in DSC for each composite and comparison with the pure ABS polymer.

This is expected, due to the different behavior of biochar at these temperatures in N and air atmospheres. As mentioned, TGA was performed until the temperature of 550 °C under nitrogen and air atmospheres for comparison purposes. Up to this temperature, the mass loss of biochar corresponds to the water content and volatile matter, including volatile (labile) carbon [47]. What remains is the fixed carbon (carbon that is not volatile) and the mineral content (ash). Further heating the biochar in an oxygen/air atmosphere will oxidize the fixed carbon and leave the ash content [48]. This is attributed to the reactivity of the oxygen/air environment, the higher the oxygen concentration, the higher the maximum reaction rate produced by the reaction. Overall, by the TGA outcome, it is evident that the inclusion of biochar does not influence the thermal stability of the ABS matrix or the rapid degradation of pure ABS, as both occur at comparable temperatures. Furthermore, the temperatures employed for filament extrusion and 3D printing do not impact the thermal stability of the materials. The residual mass was found to be in agreement with the composite loading (Fig. 4A, inset graph refers to the measurements taken in N atmosphere).

Fig. 4B presents the derivative thermogravimetry (DTG) curves. Again, the solid lines refer to the measurements taken in N atmosphere, and the dotted line to the measurements taken in air. In the air, the measurements are shifted to slightly lower temperatures. The rate pattern is similar in the 2 atm, with the addition of biochar reducing the degradation rate. Based on the TGA measurements, the Tonset, Tmax, residues at Tmax, and final residues were calculated according to instructions from the literature [49] and the values were added in Table 2. These values were for the TGA measurements conducted in nitrogen. In the air, the experiment was not completed, due to the machine's limitation to test materials up to 550 °C. Still, the differences are explained and documented in the literature, as explained above.

Fig. 4C shows the heat flow in the ABS/biochar composites as a function of temperature from differential scanning calorimetry analysis (DSC) of pure ABS. It can be observed that as the biochar loading increased, the heat flow values decreased. As the heat flow is normalized according to the sample's weight and the polymer weight in the composite is reduced as the filler loading is increased the final heat flow value is decreased. This can be attributed to the fact that the filler doesn't alter its state at the measured temperatures and thus doesn't contribute at all to the heat flow values. Fig. 4D shows the glass transition temperature (Tg, °C) measured in each composite (the Tg values were also added in Table 2). No significant changes are reported compared to pure ABS, with other composites showing higher and lower glass transition temperatures. Still, the differences are within the deviation and the statistical error.

3.3. Analysis of viscosity and melt flow rate

Fig. 5A illustrates a graph of viscosity and stress versus shear rate at 240 °C for pure ABS and ABS/biochar composites. Fig. 5B depicts the results for the melt flow rate (MFR) of pure ABS and all ABS/biochar composites in this study at 230 °C. The maximum MFR value was achieved for the pure ABS and decreased with increasing biochar loading in the composite structure. The rheology experiments presented a suitable behavior for 3D printing applications as the material presented a shear-thinning behavior that allows the material to flow smoothly through the printing nozzle but also retains its extruded shape after the printing procedure. These results also combined with the low MFR values that significantly reduce the stringing effect when the printer is executing retraction and travel moves during the printing process, make these composite materials suitable for filament 3D printing applications.

3.4. Monitoring of filament

Fig. 6A and B shows images of pure ABS and ABS/biochar 6.0 wt % filaments, respectively, during their inspection, along with the recording of their diameter during their extrusion. The filaments do not seem to have any defects, while the diameter ranges between 1.65 and 1.85 mm. Fig. 6C and D present the results obtained from the tensile strength and tensile modulus of elasticity tests, respectively, on pure ABS and ABS/biochar filaments with increasing filler concentrations up to 10 wt %. The highest values of tensile strength and tensile modulus of elasticity were determined in the case of the biochar 6.0 wt %, 25.7 %, and 22.3 % above pure ABS, respectively.

3.5. Mechanical tests

In Fig. 7, the graphs of tensile stress to strain (Fig. 7A), tensile strength (Fig. 7B), and tensile modulus of elasticity (Fig. 7C) at different filler contents are presented. Fig. 7A also displays the average stain each composite failed in the inset graph (the values shown on top of the dots are the standard deviation for the strain). The ABS/biochar composite with 4.0 wt % exhibited the highest tensile stress. Specifically, the tensile strength of the biochar with 4.0 wt % was 24.9 % greater than that of pure ABS. Additionally, the tensile

Table 2
The outcome of the TGA measurements (N atmosphere).

	Tonset (°C)	Tmax (°C)	Residual @ Tmax	Final Residual (%)	Tg (°C)
ABS Pure	404.43	426.65	54.0 %	2.0 %	106.08
ABS vs Biochar 2 wt %	405.56	429.94	52.3 %	4.1 %	103.73
ABS vs Biochar 4 wt %	406.47	431.36	52.6 %	6.2 %	105.14
ABS vs Biochar 6 wt %	401.95	426.51	53.2 %	7.9 %	104.64
ABS vs Biochar 8 wt %	401.76	428.16	53.6 %	9.8 %	106.46
ABS vs Biochar 10 wt %	398.55	425.51	54.3 %	11.9 %	106.17

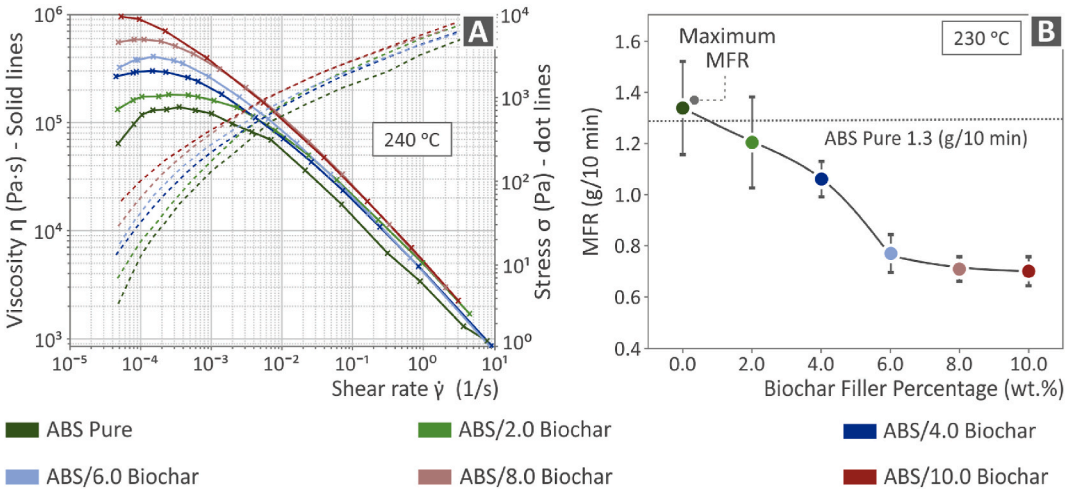

Fig. 5. **(A)** Viscosity and stress vs shear rate graph for pure ABS and ABS/biochar composites, and **(B)** MFR vs biochar filler percentage, regarding pure ABS and ABS/biochar composites.

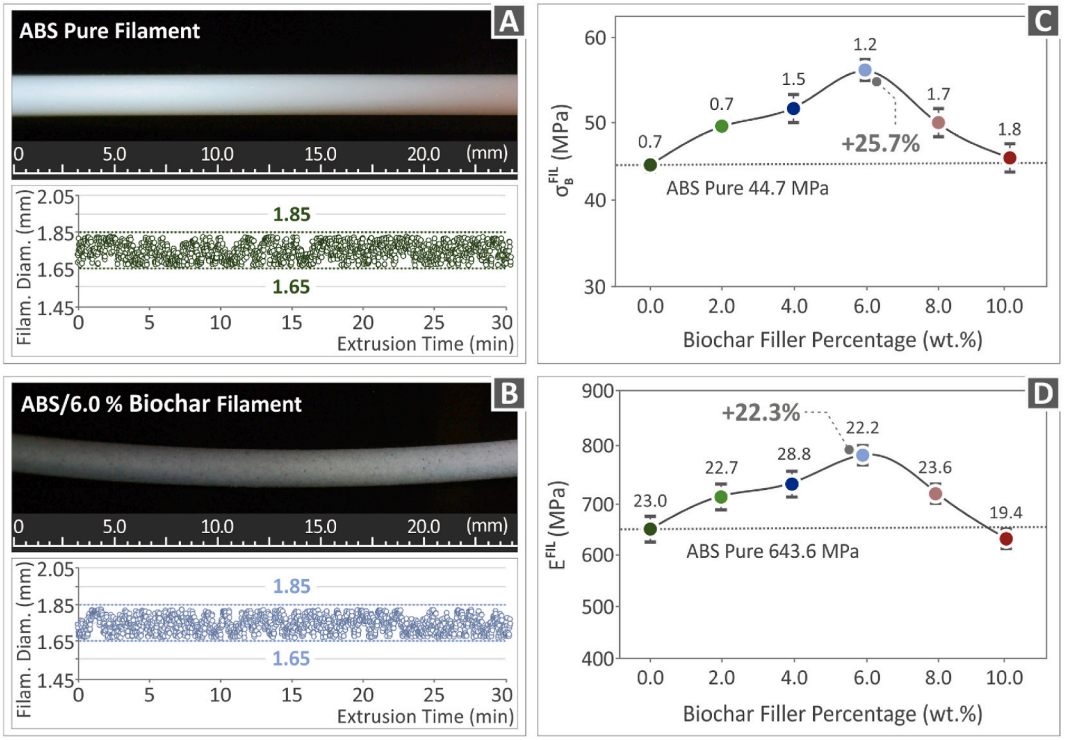

Fig. 6. Monitoring and diameter inspection of **(A)** pure ABS filament, **(B)** ABS/biochar 6.0 wt % filament, **(C)** tensile strength, and **(D)** tensile modulus of elasticity regarding the pure ABS and ABS/biochar composite filaments.

modulus of elasticity for the same composite was determined to be 25.5 % higher compared to pure ABS. Regarding the strain, a similar pattern with the strength was found. Up to 4 wt % the strain of the samples at failure increased and then started to decrease beyond this loading. The 6 wt % filled composite failed at a rather similar strain to the pure ABS. At higher loadings, the strain at failure is lower than that of the pure ABS, indicating a more brittle behavior. This in conjunction with the lower mechanical performance of these samples, suggests the saturation of the biochar filler in the matrix, which results in inferior mechanical performance in the samples.

In Fig. 8A the flexural stress-strain graphs of both pure ABS and all ABS/biochar composites are depicted, alongside two images captured before and after the flexural testing of a randomly selected specimen. The biochar composite with 4.0 wt % exhibited the highest flexural stress. Fig. 8B and C presents the results for flexural strength and flexural modulus of elasticity for all ABS/biochar

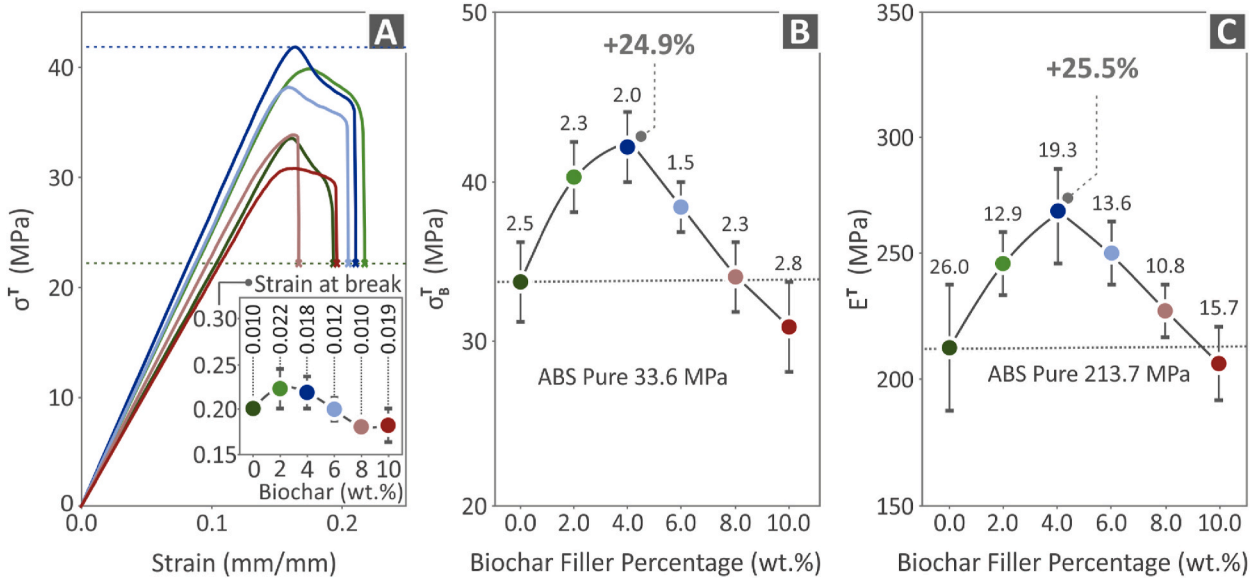

Fig. 7. Tensile tests conducted on pure ABS and ABS/biochar composites **(A)** tensile stress to strain graph and the average strain each composite failed (the values on the dots refer to the standard deviation of the strain), **(B)** tensile strength, **(C)** tensile modulus of elasticity.

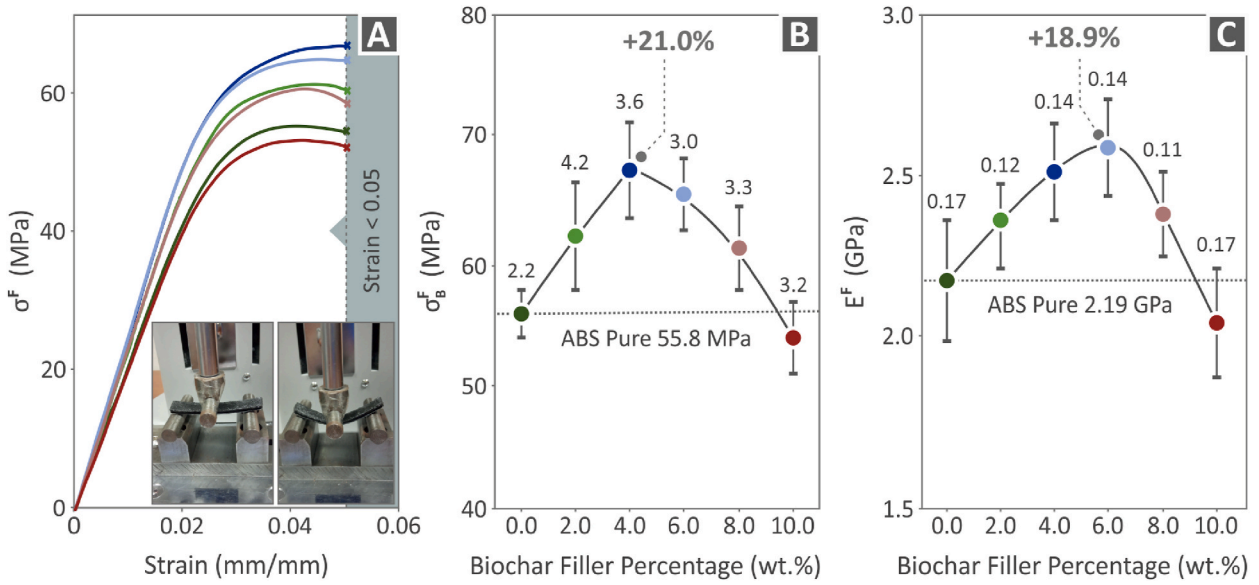

Fig. 8. Flexural tests conducted on the pure ABS and ABS/biochar composites **(A)** flexural stress to strain graph and depiction of a random specimen before and after testing, **(B)** flexural strength, **(C)** flexural modulus of elasticity.

composites. The largest reinforcements were measured in the case of the biochar 4.0 wt % regarding flexural strength (21.0 % above pure ABS) and ABS/biochar 6.0 wt % with respect to flexural modulus of elasticity (18.9 % above pure ABS).

The tensile toughness (Fig. 9A), Charpy impact strength (Fig. 9B), and microhardness (Fig. 9C) are depicted in Fig. 9. The tensile toughness of ABS/biochar 4.0 wt % was 27.9 % above pure ABS, The Charpy impact strength of pure ABS had the highest value and reduced as the biochar loading increased and the microhardness of ABS/biochar 10.0 wt % was 94.8 % higher than that of pure ABS.

3.6. *Electrical/dielectric characterization*

The real part of the dielectric permittivity (ε'), the dissipation factor, tan(δ), and the real part of ac-conductivity (σ') as a function of the frequency of pure ABS and ABS/biochar composites at various filler contents are illustrated in Fig. 10A–C. The dielectric permittivity of pure ABS shows negligible frequency dispersion over a wide frequency range, from 1 Hz to 1 MHz, and practically

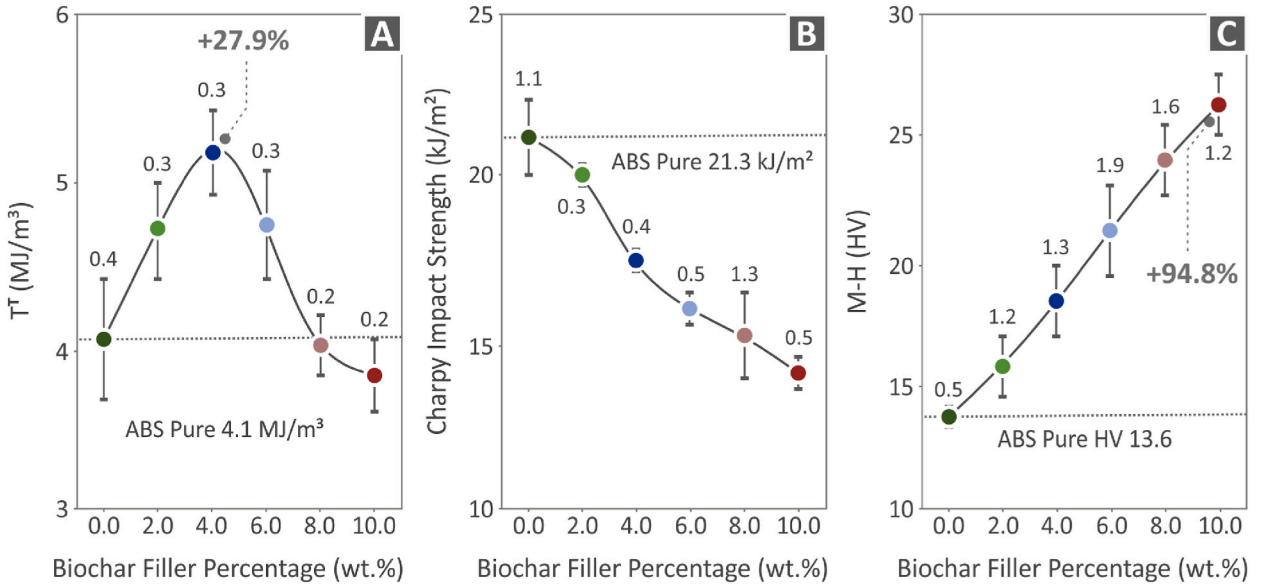

Fig. 9. Results from the conducted mechanical tests namely average values and deviation of **(A)** tensile toughness, **(B)** Charpy impact strength, **(C)** microhardness, on pure ABS, ABS/biochar 2.0 wt %, ABS/biochar 4.0 wt %, ABS/biochar 6.0 wt %, ABS/biochar 8.0 wt % and ABS/biochar 10.0 wt % specimens.

retains a constant value of 2.8–3.0, in agreement with the reported values [19,50]. In the low-frequency region, that is, below 1 Hz, an increment of ε' should be related to the ionic conductivity and the possible contribution of unwanted electrode polarization effects [51]. With a gradual increase in biochar content up to 10 %, similar frequency dependence was observed in all spectra, whereas the permittivity increased steadily in magnitude in each subsequent spectrum. The variation of ε' at high frequencies (ε_∞) with increasing filler content is shown in Fig. 10D.

The effective dielectric permittivity of a polymer composite can be predicted by considering various mixing rules that consider the dielectric permittivities of the matrix and filler materials. Here, we consider the logarithmic mixing rule and the Poon-Shin model, where the effective dielectric permittivity ε of the composite is expressed explicitly as a function of the dielectric permittivity of the polymer matrix ε_m and, filler ε_f, and volume fraction of the filler inclusions V_f [52,53]. Notably, these rules do not include any other adjusting parameters that involve the morphology of filler particles or their interactions. The corresponding equations are as follows.

$$log\ \varepsilon = (1 - V_f) log\ \varepsilon_m + V_f\ log\ \varepsilon_f \tag{4}$$

and

$$\frac{\varepsilon}{\varepsilon_m} = 1 + \frac{V_f\left(\frac{\varepsilon_f}{\varepsilon_m} - 1\right)}{V_f + \frac{1}{3}(1 - V_f)\left[\frac{\varepsilon_f}{\varepsilon_m}(1 - V_f) + V_f + 2\right]} \tag{5}$$

The theoretical predictions for the ABS/biochar composites, according to Eqs. (4) and (5) are included in Fig. 10D, showing a good agreement with the experimental values. Specifically, the logarithmic rule overestimates the effective permittivity of the composites at a low filler content, whereas the Poon-Shin model underestimates the permittivity values at a high filler content.

The frequency dependence of the dissipation factor tan(δ) of the pure ABS and its biochar composites exhibited similar spectral features, with the appearance of three distinct regions. Low values of tan(δ), below 0.01, were measured in the frequency range of 100 Hz to 1 MHz, classifying the composites as low-loss dielectric materials. However, in the low-frequency range (below 100 Hz), tan(δ) increases significantly with decreasing frequency, reaching values close to or greater than 1. At frequencies above 0.1 MHz, a relaxation feature is developed that should be related to a dipole relaxation loss process, intrinsic to the polymer matrix, as it pre-exists in the spectrum of the pure ABS specimen. The evolution of the dissipation factor with the filler content at representative frequencies in the range of 1 kHz to 1 MHz is depicted in Fig. 10E.

In general, the dielectric losses of composite material are due to contributions from dipole orientational polarization, conduction mechanisms, and interfacial polarization, which occur through the accumulation of charge carriers at the interfaces between the filler nanoparticles and matrix material [54]. Each contribution manifests itself in a different frequency range, depending on the type of charge carrier and length scale of charge accumulation. In the case of pure ABS and ABS/biochar composites, the low-frequency behavior of high dielectric losses is related to the conduction and/or interfacial polarization between the polymer and the biochar filler. Indeed, as seen in the AC conductivity spectra in Fig. 10C, a low-frequency plateau is observed for all samples at low frequencies,

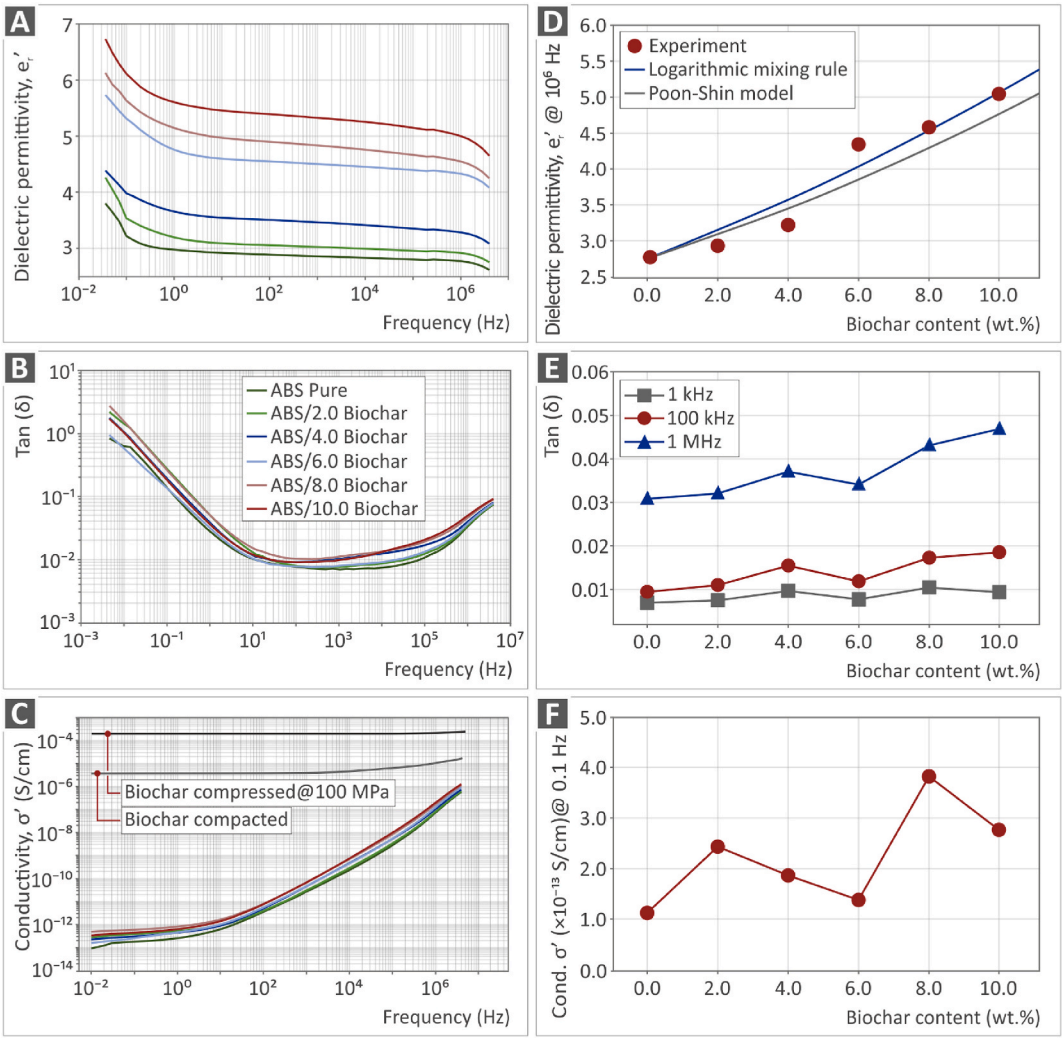

Fig. 10. Frequency dependence of (**A**) real part of dielectric permittivity, ε' (**B**) dissipation factor, tan(δ) and (**C**) real part of complex conductivity σ', of pure ABS and ABS/biochar nanocomposites at different filler concentrations. (**D**) The effective dielectric permittivity, ε_∞ (**E**) Dissipation factor at selected frequencies and (**F**) dc-conductivity, σ_{dc} as a function of biochar filler content. AC-conductivity spectra of pure biochar in compressed and compacted form are also included in (C). Solid lines in (D) represent theoretical predicted values based on the Logarithmic mixing rule and the Poon-Shin model.

suggesting that dc-conductivity is the dominant mechanism of high dielectric losses. In the high-frequency region, the intrinsic dipole polarization losses were affected by the addition of filler nanoparticles, as shown in Fig. 10E.

Regarding the spectra of AC conductivity (Fig. 10C), high dispersion is observed over a broad frequency range (~ 10–40 MHz), as AC conductivity scales with ω, a common behavior in insulating materials such as polymers. In addition, all the conductivity spectra were remarkably similar in shape, suggesting that the polymer matrix played a dominant role in the electrical response of the biochar composites. At low frequencies, the observed DC plateau in all spectra corresponds to a dc-conductivity value of the order of 10^{-13} S/cm. The dc-conductivity values, measured at 0.1 Hz, of the pure ABS and biochar composites are shown separately in Fig. 10F. DC-conductivity exhibits an oscillatory behavior with increasing filler content, ranging from 1.1×10^{-13} S/cm for pure ABS to a maximum value of 3.9×10^{-13} S/cm, at 8 % biochar content.

To evaluate the impact of biochar content on the electrical behavior of biochar composites, the ac-conductivity of raw biochar was also measured in the same frequency range. The electrical response of biochar in powder form is strongly dependent on the apparent density of the particles in the composite material and the effect of the pore space. The apparent density of biochar in compacted and highly compressed form (at 100 MPa) was found to be 0.52 g/cm^3 and 1.12 g/cm^3, respectively. The conductivity spectra of pure biochar in the compressed powder and compacted states are shown in Fig. 10C. High constant conductivity values (2×10^{-4} S/cm) were measured for the highly compressed biochar powder over almost the entire frequency range, which implies the good electrical behavior of the high-density filler. When biochar was measured in the compacted form to eliminate the pore space between the particles, a conductivity value two orders of magnitude lower than that of the highly compressed specimen was obtained (3.6×10^{-6}

S/cm). The reported conductivity values of biochar samples may vary from 10^{-2} S/m to a few hundred S/m, depending on the carbon content and temperature of the heat treatment procedure of the samples [55]. In the present study, a lower carbon content (76.7 wt %) of the raw biochar [24] results in lower values in the measured ac-conductivity spectra. Despite the relatively high measured conductivity of biochar, its incorporation into the polymeric matrix did not significantly improve the conductivity of ABS/biochar composites, even at 10 % filler content. This could be explained either by agglomeration or by a uniform distribution of the filler particles in the polymeric matrix, occurring when the filler content is below the percolation threshold, where conductive paths are formed, and the composite exhibits abruptly high electrical conductivity [56].

3.7. Analysis of specimens through SEM

Fig. 11A illustrates an SEM image of biochar at 1000 × magnification, whereas Fig. 11B depicts an SEM image of biochar at 30,000 × magnification. Fig. 11C presents the EDS analysis of biochar, where C (carbon), O (oxygen), K (potassium), and Ca (calcium) were traced. It can be observed that C was found in the highest quantity in relation to the rest of the elements, which can be justified as biochar is carbon-rich.

Fig. 12A, D, G, and J show the side surface SEM images of the pure ABS, ABS/biochar 4.0 wt %, ABS/biochar 8.0 wt %, and ABS/biochar 10.0 wt % respectively, at 150 × magnification. The fractured surfaces of the same specimens at 30 × and 1000 × magnification are shown in Fig. 12B–E, H, and K and Fig. 12C–F, I, and L respectively. The side-surface images show well-distributed layering without voids or discontinuities. The fracture surface images of the samples appear to be mostly solid, except for some microporosity, which appears in the case of pure ABS and ABS/biochar 4.0 wt % fracture at 30 × magnification, ABS/biochar 4.0 wt % fracture at 1000 × magnification, and some voids, especially at the side-points of the specimens in the case of ABS/biochar 8.0 wt % fracture at 1000 × magnification. In all three samples, the fracture area exhibited the minimum deformation, indicating brittle failure. With the addition of biochar to the composites, the fracture area became less brittle with some deformation, particularly in the higher-magnification images. This trend was maintained up to the 10 wt % composite. The fracture surface of the 10 wt % composite shows more pores and voids than the lower biochar content composites. This should have affected the mechanical performance of the samples, which is lower than the pure ABS (the one composite among the ones tested with such a response in the mechanical tests).

Fig. 13A and B shows side surface SEM images of ABS/biochar 10.0 wt % at 30 × and 150 × magnification, respectively. The 3D printed structure exhibited poor quality at this loading. Such deterioration could have adversely impacted the mechanical performance of the samples. Fig. 13C shows an EDS mapping image for the carbon element. Even at a higher loaded composite, the distribution of the biochar filler seems to be rather uniform, based on the distribution of carbon, as derived from the EDS mapping. Fig. 13D, E, and F show the fracture surface images of the ABS/biochar 10.0 wt % at 30 × , 1000 × and 30,000 × magnification are illustrated, respectively. The side-surface images show irregularly distributed layering, which includes void discontinuities and defects. In addition, the fracture surface images presented a porous and more ductile form at closer magnification.

4. Discussion

Fig. 14 summarizes the experimental findings of the mechanical tests of the pure ABS and ABS/biochar composites at 2.0, 4.0, 6.0, 8.0, and 10.0 wt % of filler content, namely tensile and flexural strength, tensile and flexural modulus of elasticity, tensile toughness, impact strength, and microhardness (left side of Fig. 14). Furthermore, the composite achieving the highest values of each one of the mechanical properties studied is depicted on the right side of Fig. 14.

The composite with the best reinforcing properties was ABS/biochar 4.0 wt % which exhibited the most substantial enhancement in

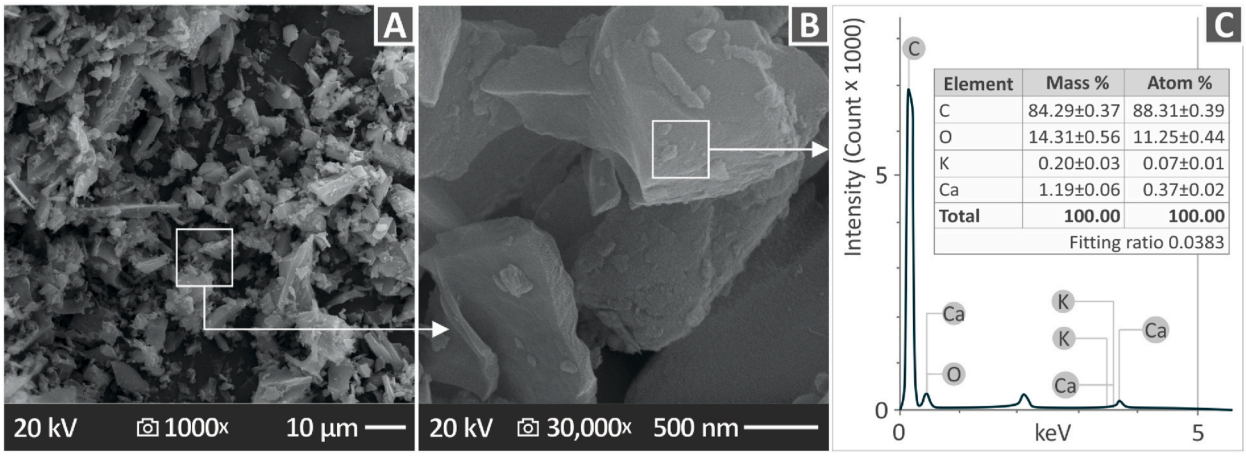

Fig. 11. Biochar raw material **(A)** images through SEM at 1000 × magnification and **(B)** 30,000 × magnification and **(C)** analysis and graph of its chemical elements by EDS.

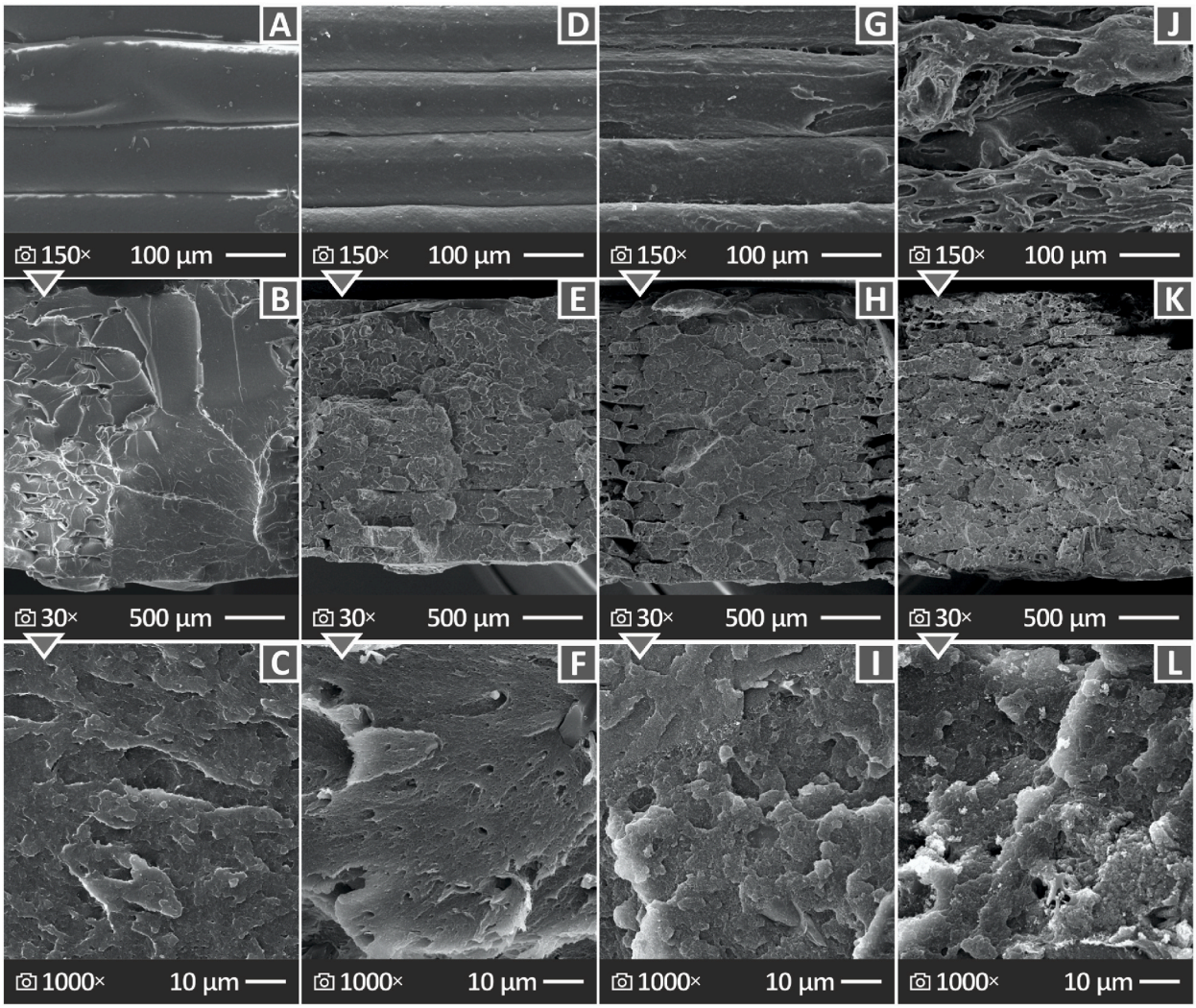

Fig. 12. SEM images at 150 × magnification of the side surface, and 30 × and at 1000 × magnification of the fracture surface for **(A–C)** pure ABS, **(D–F)** ABS/biochar 4.0 wt %, **(G–I)** ABS/biochar 8.0 wt %, **(J–L)** ABS/biochar 10.0 wt %.

four out of the seven mechanical properties examined. The tensile strength and modulus of elasticity of the ABS/biochar 4.0 wt % were 24.9 % and 25.5 % above pure ABS respectively, while flexural strength and tensile toughness, of the same composite, were increased by 21.0 % and 27.9 % in relation to pure ABS. Regarding flexural modulus of elasticity and microhardness, the results showed an 18.9 % increase at ABS/biochar 6.0 wt % and 94.8 % rise at ABS/biochar 10.0 wt % respectively. The increase in microhardness of the samples with the addition of biochar is impressive and shows the potential for using biochar in applications where high wear is expected in the parts. The Charpy impact strength was comparable to that of pure ABS, but it drastically decreased as the biochar loading increased.

According to the literature, various phenomena contribute to the reinforcement of the additives, including chemical bonding between the filler and matrix, as well as interfacial shear stress [57,58]. Regarding the impact strength, which is the ability of a material to withstand dynamic loading and was reduced by the addition of biochar in the composites, it is common in polymeric materials to have different behavior between static low-strain loads and dynamic loading. The impact strength is affected by parameters such as chain length, bonding forces, tacticity, packing, and alignment. In composites, interfacial adhesion between the polymer and the additive highly affects the impact strength [59,60]. So, the reduced performance of the composites in the impact tests, compared to the pure ABS, can be attributed to such phenomena in the samples, which need further investigation. Still, it has to be mentioned that no other additives were introduced in the composites that can improve the adhesion between the polymer and the additive since the authors wanted to show and report the clear reinforcing effect of the addition of biochar in the ABS matrix, with the specific thermomechanical process followed. Regarding the pattern of the tensile properties (strength and modulus of elasticity), the addition of the filler improved the mechanical properties up to a specific filler loading. When the mechanical properties start to constantly decrease with the further increase of the filler loading, this was an indication of saturation of the filler in the matrix, which

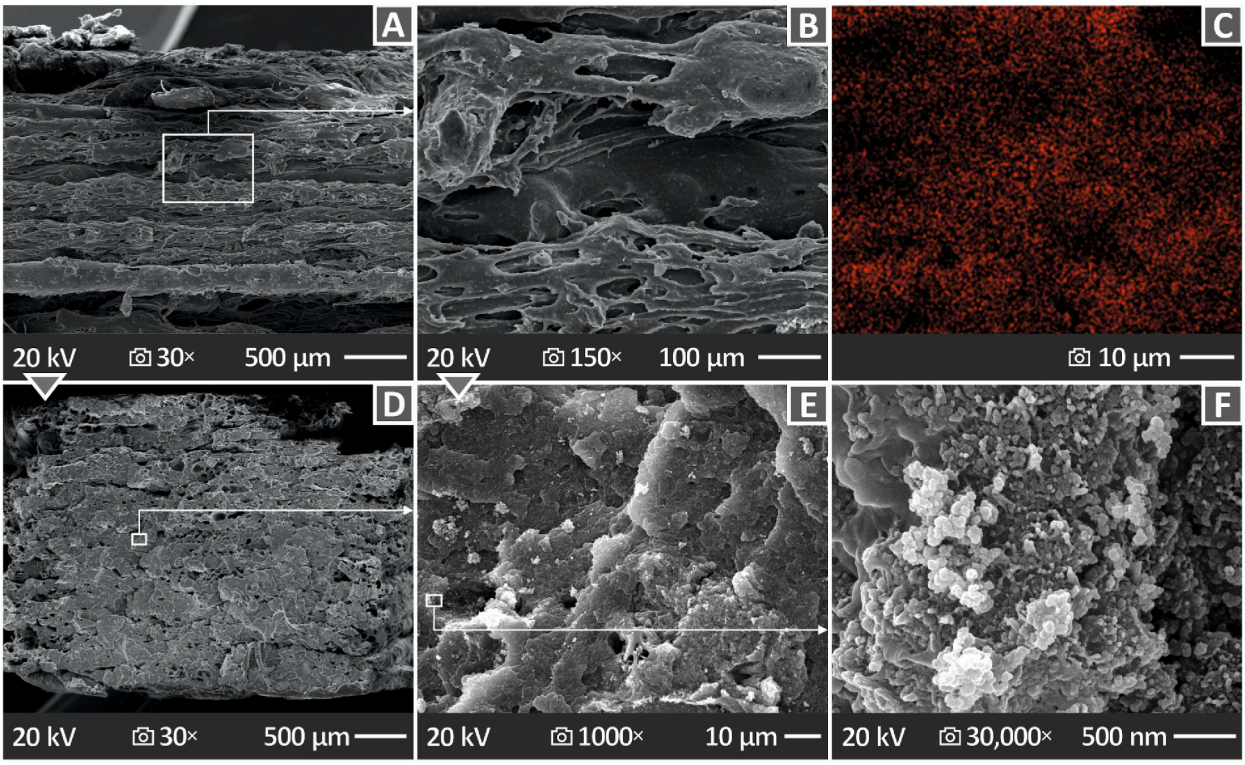

Fig. 13. SEM images of ABS/biochar 10.0 wt % **(A–B)** side surface at 30 × magnification, and fracture surface at 150 × magnification respectively, **(C)** EDS mapping image for the carbon element, **(D–F)** fracture surface at 30 × magnification, 1000 × and 30,000 × magnification.

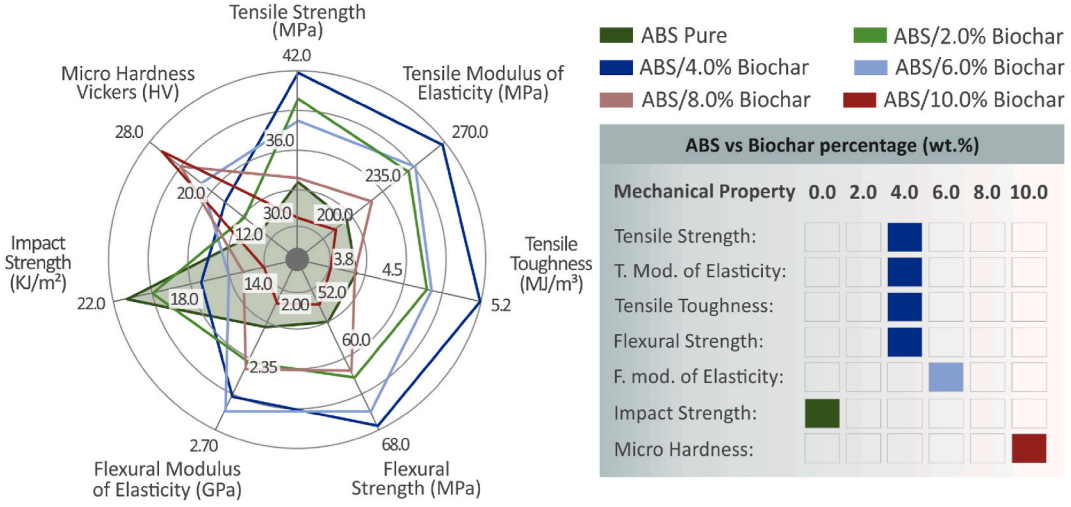

Fig. 14. Summary of the findings in the mechanical tests (left side of the figure), and presentation of the composites that achieved the highest values in each mechanical property (right side of the figure).

negatively affects the mechanical properties [61,62]. The exact saturation threshold was not determined as it was not within the scope of the study. Still, only the 10 wt % loaded composite showed tensile strength lower than the pure ABS.

The SEM images of the composites with up to 8.0 wt % biochar loading showed a mostly well-distributed layering on the side surface of the specimens, while the fracture surface only presented a few pores and voids. The ABS/biochar 10.0 wt % sample presented an uneven side surface and ductile fracture surface form with micropores, which could be probably caused by the higher filler concentration. The variations observed in the 3D printed structure due to changes in biochar loading in the composites can be attributed to the influences of the filler on the rheological properties of the ABS matrix. The reduction in the MFR suggests that the 3D

printing parameters must be properly adjusted for each composite. An increase in the nozzle temperature or an adjustment of the 3D printing speed might have prevented the formation of these defects from being formed in the 3D printed structure of the composites. This was not performed in the present study to obtain comparable results.

In another study [63], poly(ethylene terephthalate) (PET) was reinforced with biochar, and composites were created with biochar loadings of 0.5, 1.0, 3.0, and 5.0 wt %. The mixtures were utilized for the fabrication of the corresponding filaments, which were then 3D printed into the desired specimens. The mechanical, thermal, and dynamic properties of the samples were tested, and the results indicated that biochar indeed reinforced the properties of the composites. PET/biochar 0.5 wt % increased the tensile strength by 32 % compared to pure PET, while PET/biochar 5.0 wt % had a 60 % improvement over pure PET.

When biochar was added to polypropylene (PP) [64], the tensile strength decreased, probably because of the poor interaction between the biochar particles and the PP matrix, which was not the case in the present study. Similar observations were presented in a previous [65] study in which biochar was combined with PP/wood, and the tensile strength was reduced. It should be mentioned that the reduction in tensile strength was probably caused by the presence of wood, as in another investigation [66] conducted without wood, the addition of biochar to PP had a positive effect on the tensile strength of PP. Moreover, in this [67] study, biochar was combined with ultra-high molecular weight polyethylene (UHMWPE)/linear low-density polyethylene (LLDPE), and the tensile strength increased, as in the present study; however, the biochar quantity was up to 60.0 wt %.

In another study [68], the addition of up to 50.0 wt % biochar to HDPE presented a significant improvement to the flexural strength of the composite but a 70.0 wt % loading dropped the flexural strength below that of pure HDPE. This also occurred in this study but at lower biochar loadings of 4.0 wt % and 10.0 wt %. By testing the PP/biochar composites it was proved again that biochar reinforced the flexural strength of PP at a loading of 35.0 wt % [69]. In Ref. [24] the resin/biochar composites, as well as polylactic acid (PLA)/biochar composites, were created, and in both cases, biochar positively influenced the tensile strength compared to the two pure materials, especially PLA. In the case of the biochar 4.0 wt % the composite was considered as the optimum between all the loadings.

5. Conclusion

In this study, the impact of biochar as a filler on ABS was investigated by creating six different mixtures of ABS/biochar composites, namely, ABS/biochar 0.0 wt %, ABS/biochar 2.0 wt %, ABS/biochar 4.0 wt %, ABS/biochar 6.0 wt %, ABS/biochar 8.0 wt % and ABS/biochar 10.0 wt %. The corresponding filaments of each composite were fabricated and then utilized for 3D printing of the tensile, flexural, and impact specimens using the MEX method. The specimens were subjected to various tests to investigate their mechanical performance. The performance of biochar 4.0 wt % is highlighted, as it presents the most optimum properties among all composites, namely tensile (24.9 % improvement) and flexural strength (21.0 % improvement), tensile modulus of elasticity (25.5 % improvement), and toughness (27.9 % improvement). Moreover, the biochar 6.0 wt % has the highest flexural modulus of elasticity (18.9 % improvement), pure ABS has the highest impact strength, and ABS/biochar 10.0 wt % presents the highest microhardness (94.8 % improvement). An impressive increase in the microhardness of the samples with increasing biochar content in the composites should also be noted. This demonstrates the potential of using biochar as a filler in specialized applications involving high-wear environments and working conditions.

SEM was employed to examine and morphologically characterize the sides and fracture surfaces of the specimens at various magnifications. The thermomechanical and rheological behaviors and electrical conductivities of the samples were also assessed. The thermal stability of the ABS matrix remained unaffected by the incorporation of biochar in the ABS matrix. Rheological properties, such as MFR, gradually decreased with increasing biochar content of the composites. This instructs 3D printing setting adjustments for each evaluated composite. The addition of biochar increased the conductive properties of the ABS matrix, although the composites maintained their insulating behavior. Additional research can be conducted in future studies, featuring more characterization techniques and different printing parameters between the various composites. In this study, the same printing parameters were applied to all composites and pure ABS for a better comparison.

Funding

This research received no external funding.

Data availability

The raw/processed data required to reproduce these findings cannot be shared because of technical and time limitations.

CRediT authorship contribution statement

Nectarios Vidakis: Supervision, Project administration, Conceptualization. **Markos Petousis:** Writing – review & editing, Investigation. **Dimitrios Kalderis:** Formal analysis, Data curation. **Nikolaos Michailidis:** Supervision, Project administration. **Emmanuel Maravelakis:** Supervision, Project administration. **Vassilios Saltas:** Validation, Formal analysis, Data curation. **Nikolaos Bolanakis:** Formal analysis, Data curation. **Vassilis Papadakis:** Formal analysis, Data curation. **Apostolos Argyros:** Formal analysis, Data curation. **Nikolaos Mountakis:** Visualization, Formal analysis, Data curation. **Mariza Spiridaki:** Writing – original draft, Investigation.

Declaration of competing interest

The authors declare that they have no known competing financial interests or personal relationships that could have appeared to influence the work reported in this paper.

Acknowledgments

The authors would like to thank the Institute of Electronic Structure and Laser of the Foundation for Research and Technology-Hellas (IESL-FORTH) and, in particular, Ms. Aleka Manousaki for taking the SEM images presented in this work, and the Photonic Phononic and Meta-Materials Laboratory for sharing the Raman Instrumentation.

References

[1] F.R. Amin, Y. Huang, Y. He, R. Zhang, G. Liu, C. Chen, Biochar applications and modern techniques for characterization, Clean Technol. Environ. Policy 18 (2016) 1457–1473, https://doi.org/10.1007/s10098-016-1218-8.
[2] M.H. Duku, S. Gu, E. Ben Hagan, Biochar production potential in Ghana—a review, Renew. Sustain. Energy Rev. 15 (2011) 3539–3551, https://doi.org/10.1016/j.rser.2011.05.010.
[3] H.S. Kambo, A. Dutta, A comparative review of biochar and hydrochar in terms of production, physico-chemical properties and applications, Renew. Sustain. Energy Rev. 45 (2015) 359–378, https://doi.org/10.1016/j.rser.2015.01.050.
[4] M. Ahmad, A.U. Rajapaksha, J.E. Lim, M. Zhang, N. Bolan, D. Mohan, M. Vithanage, S.S. Lee, Y.S. Ok, Biochar as a sorbent for contaminant management in soil and water: a review, Chemosphere 99 (2014) 19–33, https://doi.org/10.1016/j.chemosphere.2013.10.071.
[5] M. Rizwan, S. Ali, M.F. Qayyum, M. Ibrahim, M. Zia-ur-Rehman, T. Abbas, Y.S. Ok, Mechanisms of biochar-mediated alleviation of toxicity of trace elements in plants: a critical review, Environ. Sci. Pollut. Control Ser. 23 (2016) 2230–2248, https://doi.org/10.1007/s11356-015-5697-7.
[6] J.S. Cha, S.H. Park, S.-C. Jung, C. Ryu, J.-K. Jeon, M.-C. Shin, Y.-K. Park, Production and utilization of biochar: a review, J. Ind. Eng. Chem. 40 (2016) 1–15, https://doi.org/10.1016/j.jiec.2016.06.002.
[7] K. Qian, A. Kumar, H. Zhang, D. Bellmer, R. Huhnke, Recent advances in utilization of biochar, Renew. Sustain. Energy Rev. 42 (2015) 1055–1064, https://doi.org/10.1016/j.rser.2014.10.074.
[8] D. Mohan, A. Sarswat, Y.S. Ok, C.U. Pittman, Organic and inorganic contaminants removal from water with biochar, a renewable, low cost and sustainable adsorbent – a critical review, Bioresour. Technol. 160 (2014) 191–202, https://doi.org/10.1016/j.biortech.2014.01.120.
[9] Y. Shen, Chars as carbonaceous adsorbents/catalysts for tar elimination during biomass pyrolysis or gasification, Renew. Sustain. Energy Rev. 43 (2015) 281–295, https://doi.org/10.1016/j.rser.2014.11.061.
[10] L.J. Konwar, J. Boro, D. Deka, Review on latest developments in biodiesel production using carbon-based catalysts, Renew. Sustain. Energy Rev. 29 (2014) 546–564, https://doi.org/10.1016/j.rser.2013.09.003.
[11] A.H. Lone, G.R. Najar, M.A. Ganie, J.A. Sofi, T. Ali, Biochar for sustainable soil health: a review of prospects and concerns, Pedosphere 25 (2015) 639–653, https://doi.org/10.1016/S1002-0160(15)30045-X.
[12] J. Yu, Y. Zhao, Y. Li, Utilization of corn cob biochar in a direct carbon fuel cell, J. Power Sources 270 (2014) 312–317, https://doi.org/10.1016/j.jpowsour.2014.07.125.
[13] A. Elleuch, A. Boussetta, J. Yu, K. Halouani, Y. Li, Experimental investigation of direct carbon fuel cell fueled by almond shell biochar: Part I. Physico-chemical characterization of the biochar fuel and cell performance examination, Int. J. Hydrogen Energy 38 (2013) 16590–16604, https://doi.org/10.1016/j.ijhydene.2013.08.090.
[14] R.K. Gupta, M. Dubey, P. Kharel, Z. Gu, Q.H. Fan, Biochar activated by oxygen plasma for supercapacitors, J. Power Sources 274 (2015) 1300–1305, https://doi.org/10.1016/j.jpowsour.2014.10.169.
[15] J. Jiang, L. Zhang, X. Wang, N. Holm, K. Rajagopalan, F. Chen, S. Ma, Highly ordered macroporous woody biochar with ultra-high carbon content as supercapacitor electrodes, Electrochim. Acta 113 (2013) 481–489, https://doi.org/10.1016/j.electacta.2013.09.121.
[16] T. Huggins, H. Wang, J. Kearns, P. Jenkins, Z.J. Ren, Biochar as a sustainable electrode material for electricity production in microbial fuel cells, Bioresour. Technol. 157 (2014) 114–119, https://doi.org/10.1016/j.biortech.2014.01.058.
[17] A. Kacprzak, R. Kobyłecki, R. Włodarczyk, Z. Bis, The effect of fuel type on the performance of a direct carbon fuel cell with molten alkaline electrolyte, J. Power Sources 255 (2014) 179–186, https://doi.org/10.1016/j.jpowsour.2014.01.012.
[18] M.-M. Titirici, RobinJ. White, C. Falco, M. Sevilla, Black perspectives for a green future: hydrothermal carbons for environment protection and energy storage, Energy Environ. Sci. 5 (2012) 6796, https://doi.org/10.1039/c2ee21166a.
[19] N. Vidakis, A. Maniadi, M. Petousis, M. Vamvakaki, G. Kenanakis, E. Koudoumas, Mechanical and electrical properties investigation of 3D-printed acrylonitrile–butadiene–styrene graphene and carbon nanocomposites, J. Mater. Eng. Perform. 29 (2020) 1909–1918, https://doi.org/10.1007/s11665-020-04689-x.
[20] N. Vidakis, M. Petousis, K. Savvakis, A. Maniadi, E. Koudoumas, A comprehensive investigation of the mechanical behavior and the dielectrics of pure polylactic acid (PLA) and PLA with graphene (GnP) in fused deposition modeling (FDM), Int. J. Plast. Technol. 23 (2019) 195–206, https://doi.org/10.1007/s12588-019-09248-1.
[21] P. Rani, K. Deshmukh, J. Kadlec, T. V Krishna Karthik, S.K. Khadheer Pasha, Dielectric properties of graphene/nano-Fe2O3 filled poly (vinyl alcohol)/Chitosan blends, Mater. Chem. Phys. 295 (2023) 126986, https://doi.org/10.1016/j.matchemphys.2022.126986.
[22] Y. Zhang, T. Hu, R. Hu, S. Jiang, C. Zhang, H. Hou, Thermal, mechanical and dielectric properties of polyimide composite films by in-situ reduction of fluorinated graphene, Molecules 27 (2022), https://doi.org/10.3390/molecules27248896.
[23] A. Maniadi, M. Vamvakaki, M. Petousis, N. Vidakis, M. Suchea, M. Sevastaki, Z. Viskadourakis, G. Kenanakis, E. Koudoumas, Effect of zinc oxide concentration on the dielectric properties of 3D printed acrylonitrile butadiene styrene nanocomposites, in: 2019 International Semiconductor Conference (CAS), 2019, pp. 221–224, https://doi.org/10.1109/SMICND.2019.8923905.
[24] N. Vidakis, D. Kalderis, M. Petousis, E. Maravelakis, N. Mountakis, N. Bolanakis, V. Papadakis, Biochar filler in MEX and VPP additive manufacturing: characterization and reinforcement effects in polylactic acid and standard grade resin matrices, Biochar 5 (2023) 39, https://doi.org/10.1007/s42773-023-00238-6.
[25] N. Vidakis, M. Petousis, D. Kalderis, N. Michailidis, E. Maravelakis, V. Saltas, N. Bolanakis, V. Papadakis, M. Spiridaki, A. Argyros, Reinforced HDPE with optimized biochar content for material extrusion additive manufacturing: morphological, rheological, electrical, and thermomechanical insights, Biochar 6 (2024) 37, https://doi.org/10.1007/s42773-024-00314-5.
[26] H.K. Dave, R.T. Karumuri, A.R. Prajapati, S.R. Rajpurohit, Specific energy absorption during compression testing of ABS and FPU parts fabricated using LCD-SLA based 3D printer, Rapid Prototyp. J. 28 (2022) 1530–1540, https://doi.org/10.1108/RPJ-04-2021-0075.
[27] N. Vidakis, M. Petousis, E. Velidakis, M. Liebscher, V. Mechtcherine, L. Tzounis, On the strain rate sensitivity of fused filament fabrication (Fff) processed pla, abs, petg, pa6, and pp thermoplastic polymers, Polymers 12 (2020) 1–15, https://doi.org/10.3390/polym12122924.
[28] M. Petousis, N. Michailidis, V.M. Papadakis, A. Korlos, N. Mountakis, A. Argyros, E. Dimitriou, C. Charou, A. Moutsopoulou, N. Vidakis, Optimizing the rheological and thermomechanical response of acrylonitrile butadiene styrene/silicon nitride nanocomposites in material extrusion additive manufacturing, Nanomaterials 13 (2023) 1588, https://doi.org/10.3390/nano13101588.

[29] N. Vidakis, A. Moutsopoulou, M. Petousis, N. Michailidis, C. Charou, V. Papadakis, N. Mountakis, E. Dimitriou, A. Argyros, Rheology and thermomechanical evaluation of additively manufactured acrylonitrile butadiene styrene (ABS) with optimized tungsten carbide (WC) nano-ceramic content, Ceram. Int. (2023), https://doi.org/10.1016/j.ceramint.2023.08.144.
[30] N. Dhakal, X. Wang, C. Espejo, A. Morina, N. Emami, Impact of processing defects on microstructure, surface quality, and tribological performance in 3D printed polymers, J. Mater. Res. Technol. 23 (2023) 1252–1272, https://doi.org/10.1016/j.jmrt.2023.01.086.
[31] N. Vidakis, A. Moutsopoulou, M. Petousis, N. Michailidis, C. Charou, V. Papadakis, N. Mountakis, E. Dimitriou, A. Argyros, Rheology and thermomechanical evaluation of additively manufactured acrylonitrile butadiene styrene (ABS) with optimized tungsten carbide (WC) nano-ceramic content, Ceram. Int. 49 (2023) 34742–34756, https://doi.org/10.1016/j.ceramint.2023.08.144.
[32] M. Petousis, N. Vidakis, N. Mountakis, E. Karapidakis, A. Moutsopoulou, A. Moutsopoulou amalia, Compressive response versus power consumption of acrylonitrile butadiene styrene in material extrusion additive manufacturing : the impact of seven critical control parameters, J. Adv. Manuf. Technol. (2023), https://doi.org/10.1007/s00170-023-11202-w.
[33] N. Vidakis, C.N. David, M. Petousis, D. Sagris, N. Mountakis, Optimization of key quality indicators in material extrusion 3D printing of acrylonitrile butadiene styrene: the impact of critical process control parameters on the surface roughness, dimensional accuracy, and porosity, Mater. Today Commun. 34 (2022) 105171, https://doi.org/10.1016/j.mtcomm.2022.105171.
[34] N. Vidakis, M. Petousis, A. Maniadi, E. Koudoumas, A. Vairis, J. Kechagias, Sustainable additive manufacturing: mechanical response of acrylonitrile-butadiene-styrene over multiple recycling processes, Sustainability (Switzerland) 12 (2020) 3568, https://doi.org/10.3390/su12093568.
[35] T. Tsubota, S. Tsuchiya, T. Kusumoto, D. Kalderis, Assessment of biochar produced by flame-curtain pyrolysis as a precursor for the development of an efficient electric double-layer capacitor, Energies (Basel) 14 (2021) 7671, https://doi.org/10.3390/en14227671.
[36] Z. Movasaghi, S. Rehman, I.U. Rehman, Raman spectroscopy of biological tissues, Appl. Spectrosc. Rev. 42 (2007) 493–541, https://doi.org/10.1080/05704920701551530.
[37] B.H. Stuart, Temperature studies of polycarbonate using Fourier transform Raman spectroscopy, Polym. Bull. 36 (1996) 341–346, https://doi.org/10.1007/BF00319235.
[38] M. Makarem, C.M. Lee, K. Kafle, S. Huang, I. Chae, H. Yang, J.D. Kubicki, S.H. Kim, Probing cellulose structures with vibrational spectroscopy, Cellulose 26 (2019) 35–79, https://doi.org/10.1007/s10570-018-2199-z.
[39] D. Giordano, J.K. Russell, D. González-García, D. Bersani, D.B. Dingwell, C. Del Negro, Raman spectroscopy from laboratory and proximal to remote sensing: a tool for the volcanological sciences, Rem. Sens. 12 (2020) 805, https://doi.org/10.3390/rs12050805.
[40] V. Resta, G. Quarta, M. Lomascolo, L. Maruccio, L. Calcagnile, Raman and Photoluminescence spectroscopy of polycarbonate matrices irradiated with different energy 28Si+ ions, Vacuum 116 (2015) 82–89, https://doi.org/10.1016/j.vacuum.2015.03.005.
[41] B.H. Stuart, Temperature studies of polycarbonate using Fourier transform Raman spectroscopy, Polym 36 (1996) 341–346, https://doi.org/10.1007/BF00319235.
[42] Z. Lin, X. Guo, Z. He, X. Liang, M. Wang, G. Jin, M.M. W, G.J. Lin, Z. N, X.M. Guo, Z.P. He, X.R. Liang, Z. Lin, X. Guo, Z. He, X. Liang, M. Wang, G. Jin, Thermal degradation kinetics study of molten polylactide based on Raman spectroscopy, Polym. Eng. Sci. 61 (2021) 201–210, https://doi.org/10.1002/pen.25568.
[43] C. Zimmerer, I. Matulaitiene, G. Niaura, U. Reuter, A. Janke, R. Boldt, V. Sablinskas, G. Steiner, Nondestructive characterization of the polycarbonate - octadecylamine interface by surface enhanced Raman spectroscopy, Polym. Test. 73 (2019) 152–158, https://doi.org/10.1016/j.polymertesting.2018.11.023.
[44] A.V. Spivak, Y.A. Litvin, A.V. Shushkanova, V.Y.u.S. Litvin, Diamond formation in carbonate-silicate-sulfide-carbon melts: Raman- and IR-microspectroscopy, Eur. J. Mineral 20 (2008) 341–347, https://doi.org/10.1127/0935-1221/2008/0020-1818.
[45] B.K.M. Luiz, R.D.M.C. Amboni, L.H.M. Prates, J. Roberto Bertolino, A.T.N. Pires, Influence of drinks on resin composite: evaluation of degree of cure and color change parameters, Polym. Test. 26 (2007) 438–444, https://doi.org/10.1016/j.polymertesting.2006.12.005.
[46] E. Gatin, S.-M. Iordache, E. Matei, C.-R. Luculescu, A.-M. Iordache, C.E.A. Grigorescu, R.R. Ilici, Raman spectroscopy as spectral tool for assessing the degree of conversion after curing of two resin-based materials used in restorative dentistry, Diagnostics 12 (2022) 1993, https://doi.org/10.3390/diagnostics12081993.
[47] W.-W. Tian, F. Xu, S.-J. Xing, R. Wu, Z.-Y. Yuan, Comprehensive study on the thermal decomposition process of waste tobacco leaves and stems to investigate their bioenergy potential: kinetic, thermodynamic, and biochar analysis, Thermochim. Acta 723 (2023) 179473, https://doi.org/10.1016/j.tca.2023.179473.
[48] S. Elkhalifa, P. Parthasarathy, H.R. Mackey, T. Al-Ansari, O. Elhassan, S. Mansour, G. McKay, Biochar development from thermal TGA studies of individual food waste vegetables and their blended systems, Biomass Convers. Biorefin. (2022), https://doi.org/10.1007/s13399-022-02441-0.
[49] M. Kervran, C. Vagner, M. Cochez, M. Ponçot, M.R. Saeb, H. Vahabi, Thermal degradation of polylactic acid (PLA)/polyhydroxybutyrate (PHB) blends: a systematic review, Polym. Degrad. Stabil. 201 (2022) 109995, https://doi.org/10.1016/j.polymdegradstab.2022.109995.
[50] V. Francis, P.K. Jain, 3D printed polymer dielectric substrates with enhanced permittivity by nanoclay inclusion, Virtual Phys. Prototyp. 12 (2017) 107–115, https://doi.org/10.1080/17452759.2017.1312466.
[51] V. Saltas, F. Vallianatos, E. Gidarakos, Charge transport in diatomaceous earth studied by broadband dielectric spectroscopy, Appl. Clay Sci. 80–81 (2013) 226–235, https://doi.org/10.1016/j.clay.2013.02.028.
[52] R. Simpkin, Derivation of lichtenecker's logarithmic mixture formula from maxwell's equations, IEEE Trans. Microw. Theor. Tech. 58 (2010) 545–550, https://doi.org/10.1109/TMTT.2010.2040406.
[53] Y.M. Poon, F.G. Shin, A simple explicit formula for the effective dielectric constant of binary 0-3 composites, J. Mater. Sci. 39 (2004) 1277–1281, https://doi.org/10.1023/B:JMSC.0000013886.21054.e4.
[54] W. Zhou, Z. Wang, L. Dong, X. Sui, Q. Chen, Dielectric properties and thermal conductivity of PVDF reinforced with three types of Zn particles, Compos Part A Appl Sci Manuf 79 (2015) 183–191, https://doi.org/10.1016/j.compositesa.2015.09.004.
[55] R.S. Gabhi, D.W. Kirk, C.Q. Jia, Preliminary investigation of electrical conductivity of monolithic biochar, Carbon N Y 116 (2017) 435–442, https://doi.org/10.1016/j.carbon.2017.01.069.
[56] Z.-M. Dang, J.-K. Yuan, J.-W. Zha, T. Zhou, S.-T. Li, G.-H. Hu, Fundamentals, processes and applications of high-permittivity polymer–matrix composites, Prog. Mater. Sci. 57 (2012) 660–723, https://doi.org/10.1016/j.pmatsci.2011.08.001.
[57] M. Chan, K. Lau, T. Wong, M. Ho, D. Hui, Mechanism of reinforcement in a nanoclay/polymer composite, Compos. B Eng. 42 (2011) 1708–1712, https://doi.org/10.1016/j.compositesb.2011.03.011.
[58] W. Han, J. Zhou, Q. Shi, Research progress on enhancement mechanism and mechanical properties of FRP composites reinforced with graphene and carbon nanotubes, Alex. Eng. J. 64 (2023) 541–579, https://doi.org/10.1016/j.aej.2022.09.019.
[59] W.G. Perkins, Polymer toughness and impact resistance, Polym. Eng. Sci. 32 (1999) 2445–2460, https://doi.org/10.1002/pen.11632.
[60] A.Y. Al-Maharma, P. Sendur, Review of the main factors controlling the fracture toughness and impact strength properties of natural composites, Mater. Res. Express 6 (2019) 022001, https://doi.org/10.1088/2053-1591/aaec28.
[61] Y. Zare, K.Y. Rhee, The mechanical behavior of CNT reinforced nanocomposites assuming imperfect interfacial bonding between matrix and nanoparticles and percolation of interphase regions, Compos. Sci. Technol. 144 (2017) 18–25, https://doi.org/10.1016/j.compscitech.2017.03.012.
[62] M.Z. Rong, M.Q. Zhang, Y.X. Zheng, H.M. Zeng, K. Friedrich, Improvement of tensile properties of nano-SiO2/PP composites in relation to percolation mechanism, Polymer (Guildf) 42 (2001) 3301–3304, https://doi.org/10.1016/S0032-3861(00)00741-2.
[63] M. Idrees, S. Jeelani, V. Rangari, Three-Dimensional-printed sustainable biochar-recycled PET composites, ACS Sustain. Chem. Eng. 6 (2018) 13940–13948, https://doi.org/10.1021/acssuschemeng.8b02283.
[64] A.M. Poulose, A.Y. Elnour, A. Anis, H. Shaikh, S.M. Al-Zahrani, J. George, M.I. Al-Wabel, A.R. Usman, Y.S. Ok, D.C.W. Tsang, A.K. Sarmah, Date palm biochar-polymer composites: an investigation of electrical, mechanical, thermal and rheological characteristics, Sci. Total Environ. 619–620 (2018) 311–318, https://doi.org/10.1016/j.scitotenv.2017.11.076.
[65] O. Das, A.K. Sarmah, D. Bhattacharyya, A novel approach in organic waste utilization through biochar addition in wood/polypropylene composites, Waste Manag. 38 (2015) 132–140, https://doi.org/10.1016/j.wasman.2015.01.015.

[66] O. Das, D. Bhattacharyya, D. Hui, K.-T. Lau, Mechanical and flammability characterisations of biochar/polypropylene biocomposites, Compos. B Eng. 106 (2016) 120–128, https://doi.org/10.1016/j.compositesb.2016.09.020.
[67] S. Li, A. Huang, Y.-J. Chen, D. Li, L.-S. Turng, Highly filled biochar/ultra-high molecular weight polyethylene/linear low density polyethylene composites for high-performance electromagnetic interference shielding, Compos. B Eng. 153 (2018) 277–284, https://doi.org/10.1016/j.compositesb.2018.07.049.
[68] Q. Zhang, M.U. Khan, X. Lin, H. Cai, H. Lei, Temperature varied biochar as a reinforcing filler for high-density polyethylene composites, Compos. B Eng. 175 (2019) 107151, https://doi.org/10.1016/j.compositesb.2019.107151.
[69] O. Das, D. Bhattacharyya, A.K. Sarmah, Sustainable eco–composites obtained from waste derived biochar: a consideration in performance properties, production costs, and environmental impact, J. Clean. Prod. 129 (2016) 159–168, https://doi.org/10.1016/j.jclepro.2016.04.088.